



## Research article

# Multiview spatial compounding using lens-based photoacoustic imaging system<sup>☆</sup>

Kalloor Joseph Francis<sup>a,1,\*</sup>, Bhargava Chinni<sup>b</sup>, Sumohana S. Channappayya<sup>a</sup>,  
Rajalakshmi Pachamuthu<sup>a</sup>, Vikram S. Dogra<sup>b</sup>, Naval Gund Rao<sup>c,\*\*</sup>

<sup>a</sup> Department of Electrical Engineering, Indian Institute of Technology Hyderabad, 502285, India

<sup>b</sup> Department of Imaging Sciences, University of Rochester Medical Center, 601 Elmwood Ave, Rochester, NY 14642, USA

<sup>c</sup> Chester F. Carlson Center for Imaging Science, Rochester Institute of Technology, 54 Lomb Memorial Drive, Rochester, NY 14623, USA

## ARTICLE INFO

## Keywords:

Acoustic lens  
Photoacoustic camera  
Point Spread Function  
Resolution  
Refocusing  
Spatial compounding

## ABSTRACT

Recently, an acoustic lens has been proposed for volumetric focusing as an alternative to conventional reconstruction algorithms in Photoacoustic (PA) Imaging. Acoustic lens can significantly reduce computational complexity and facilitate the implementation of real-time and cost-effective systems. However, due to the fixed focal length of the lens, the Point Spread Function (PSF) of the imaging system varies spatially. Furthermore, the PSF is asymmetric, with the lateral resolution being lower than the axial resolution. For many medical applications, such as *in vivo* thyroid, breast and small animal imaging, multiple views of the target tissue at varying angles are possible. This can be exploited to reduce the asymmetry and spatial variation of system the PSF with simple spatial compounding. In this article, we present a formulation and experimental evaluation of this technique. PSF improvement in terms of resolution and Signal to Noise Ratio (SNR) with the proposed spatial compounding is evaluated through simulation. Overall image quality improvement is demonstrated with experiments on phantom and *ex vivo* tissue. When multiple views are not possible, an alternative residual refocusing algorithm is proposed. The performances of these two methods, both separately and in conjunction, are compared and their practical implications are discussed.

## 1. Introduction

Photoacoustic (PA) imaging is a new modality that is beginning to make a transition into the clinical arena. PA imaging systems that are capable of providing functional images of thyroid, breast and skin are under development [1]. In PA imaging, pulsed laser light excites Ultrasound (US) signal with an amplitude proportional to optical absorption of the tissue due to the thermoelastic effect. Afforded by US-based imaging, PA images, provide high optical absorption contrast at superior resolution [1].

Image quality, technical feasibility and computational efficiency are important factors to be considered in designing a PA imaging system, especially when we are dealing with large three dimensional (3D) datasets. 3D reconstruction algorithms in general demand significant computational post-processing and memory. For real-time

implementation, costly and dedicated hardware is needed, especially for volumetric three dimensional (3D) imaging, as in high-end PA imaging systems like VisualSonics Vevo 660TM (VisualSonics Inc., Toronto, Canada) and Endra Nexus 128 (USA). Acoustic lens based PA imaging is a potential alternative to conventional computational reconstruction based imaging. The lens-based approach eliminates computational and memory intense reconstruction and offers a simple, low-cost and real-time implementation [2,3].

An acoustic lens-based PA imaging was first proposed by He et al. [4] in 2006. A unit magnification lens-based PA system and a peak holding method for image formation can be found in [5–7]. Adapting the unit magnification system design in 2010, Valluru et al. proposed a 3D printed imaging probe which enabled a compact system known as a PA camera [2]. The utility of a PA camera in *ex vivo* studies was presented by Dogra et al. in 2014 [8]. Multi-spectral PA imaging using the PA camera allowed

<sup>☆</sup> This work was supported by grant from NIBIB, NIH through grant no. 1R15EB019726-01. We greatly acknowledge Lang memorial foundation for providing financial support for the laser.

\* Corresponding author.

\*\* Principal corresponding author.

E-mail addresses: [ee14resch12001@iith.ac.in](mailto:ee14resch12001@iith.ac.in) (K.J. Francis), [narpci@cis.rit.edu](mailto:narpci@cis.rit.edu) (N. Rao).

<sup>1</sup> Supported by the US Fulbright program.

the classification of malignant, benign and normal human prostate tissue [9–11]. However, all of the above studies have used a time gating approach to image the optimally focused depth plane as a two dimensional (2D) C-scan image (planar view of the object plane parallel to imaging plane). The focusing nature of the lens at other depth planes had to be investigated. The first attempt in volumetric PA imaging using 3 point targets with 4F aluminum lens and CCD camera system was presented by Niederhauser in 2004 [12]. A preliminary study on imaging a phantom having targets at multiple depths using acoustic lens was presented by Chen et al. in 2010 [13]. These volumetric imaging methods utilized the movement of the sensor plane to focus and image multiple depths or used a fixed sensor for a small volume around 2F plane [13,14]. An extensive theoretical and experimental study of PA camera PSF at different depth planes and off-axis locations was conducted by Francis et al. in 2017 [3]. It was shown that the axial resolution of the system is determined by the transducer impulse response while the lateral resolution is mainly determined by the lens parameters and the center frequency of the transducer. For such a system, typically the 2D PSF is not circularly symmetric, its width perpendicular to the lens axis is larger than its width in the direction of the lens axis. Furthermore, the PSF varies significantly for depth planes in the 3D object that is in front of or behind the optimally focused depth plane.

In this article, we propose and evaluate a unique 3D PA imaging system prototype that produces approximately spherical 1 millimeter resolution that is uniform throughout a  $4\text{ cm} \times 4\text{ cm} \times 4\text{ cm}$  imaging volume. The system consists of two parts. First is a lens based 3D US signal focusing device, which we refer to here as the PA camera and second is the computationally efficient post-processing methodology that works on the data acquired by the PA camera. The details of the PA imaging camera are given in [2,3,15,16]. The focus of this article is on the second part of the prototype, that is developing a computationally efficient method that improves the 3D image quality by rendering the system PSF uniform throughout the investigated tissue volume. As a primary contribution, we evaluate a simple spatial compounding (SC) technique. This is the first time it is being used to improve the resolution of point targets in lens-based PA imaging. Different angular views taken by the PA camera of the same imaging volume are averaged after appropriate data correction and registration. In addition, we investigate the use of another technique we have developed that can be applied to each of the angular views of the PA camera before SC. The details of this technique, which we will refer to henceforth as residual refocusing, can be found in [17]. The additional blurring or defocusing of depth planes in front and behind the optimally focused plane that we mentioned earlier, can be reversed by this technique. Because SC and residual refocusing improve the PSF in different ways, we have also investigated the image quality improvement when they are used in conjunction. First, the processing techniques and their improvement potential are evaluated quantitatively on the simulated PSF data acquired from a 2D simulation of the entire PA camera system. PSFs were simulated for different depth planes, ranging in distance up to 2 cm on either side of the best focal plane. Finally, we demonstrate experimentally the improvements on 3D phantoms with multiple PA targets and a simulated lesion in *ex-vivo* chicken breast tissue.

## 2. Background

This section briefly introduces the reader to the generic features of the PA imaging camera, its PSF and limitations. Literature review on SC and residual refocusing is also presented in this section.

### 2.1. PA camera system

In this system, photoacoustically generated US waves from absorbers within a tissue volume are allowed to propagate towards an acoustic lens. The lens is able to focus the waves on to a well-defined image plane where the two dimensional (2D) US transducer array elements capture and store the A-line signals from independent digital channels. A-line signals are

one-dimensional time series where the relative arrival time of a focused wavefront represents the distance the wave has traveled from the source. By using an acoustic lens in a setup similar to an optical camera, we can eliminate the need for 3D reconstruction algorithms or dedicated hardware similar to that used in time delay implementation of US beamforming in receive mode [18,3]. Both lens-based focusing and digital beamforming methods produce similar, but not identical results. The differences are worth noting. While in the former case, the focusing process takes place in a continuous space-time domain and happens in real time, in the latter case, it takes place in a sampled space-time domain as a post-processing step. Hence one needs to consider minimizing sampling artifacts in beamforming. In both cases, the resolution and signal-to-noise (SNR) metrics are directly proportional to the aperture size, assuming all other factors such as frequency, sensor element size and spacing, etc. are equal. In beamforming, the total area covered by actively receiving transducer array elements represent its aperture, while for the lens based focusing it is the diameter of the lens. To improve the quality metrics, increasing the lens diameter is much more cost effective than increasing the number of active digital channels [3].

Let us look into the focusing action of the lens in more detail. Consider a point source of PA signal at a distance from the center of the lens. The spherical waves from the source propagate through a water-filled medium towards the lens. Assume a lens with thickness  $\Delta_0$  and focal length  $F$ . Let  $2F$  be the distance from the center of the lens, then the phase change introduced by the lens at radius  $r_L$  from the center can be written as [3],

$$\Phi(r_L) = e^{ik_0\Delta_0} e^{-\frac{ik_0 r_L^2}{2F}}, \quad (1)$$

with  $k_0 = 2\pi f_0/c_0$ , where a monochromatic approach is used with  $f_0 = f_c$  taken as the center frequency of the transducer.  $c_0$  is the speed of sound in the medium. This additional phase converts the diverging wavefront to a converging one which, as it propagates, comes to focus at a distance  $I$  on the other side of the lens.  $O$  and  $I$  are related by the well known lens equation  $\frac{1}{O} + \frac{1}{I} = \frac{1}{F}$ . We consider a geometry where the object distance is at  $2F$  and consequently the focused image is formed at a distance of  $2F$ , giving us a magnification of  $-1$ . We keep the transducer array fixed at this location. In addition to the phase change, the lens also acts to limit the aperture. For a given lens of radius  $\rho$ , the aperture function is,

$$\Psi(r_L) = \begin{cases} 1, & \text{if } r_L \leq \rho \\ 0, & \text{otherwise.} \end{cases} \quad (2)$$

This limited aperture of the lens, along with finite bandwidth filtering by the frequency response of the transducer, is responsible for the finite size of the system PSF.

Another limiting aspect of the lens based system is that the spatial resolution based on the system point-spread-function (PSF) is not uniform throughout the imaging volume. This happens because the lens has a fixed focus, therefore PA signals from point sources outside the well defined focal plane suffer from a deterministic degree of blurring or defocusing. Consider a PA signal coming from a point source that is located at an object distance  $O = 2F - 20\text{ mm}$ . To fully focus this signal, either the lens, or the transducer array or both must be moved, so as to satisfy the lens equation. This is currently not possible because, in order to maintain technical simplicity and real-time capability, we are keeping the transducer array fixed at  $2F$  distance from the lens. Therefore a somewhat defocused PSF is formed with the signal received by the array, albeit at a different arrival time compared to the source at  $2F$ . If a volumetric image is generated from the data acquired by the PA camera, the best quality will be at plane with gradually increasing degradation expected for other planes. Correcting this degradation is the main objective of this paper.

### 2.2. Spatial compounding

SC has been widely used in US imaging to reduce speckle and improve contrast to noise resolution (CNR) [19]. Spatial compounding involves acquiring subimages from different angles and combining them to form

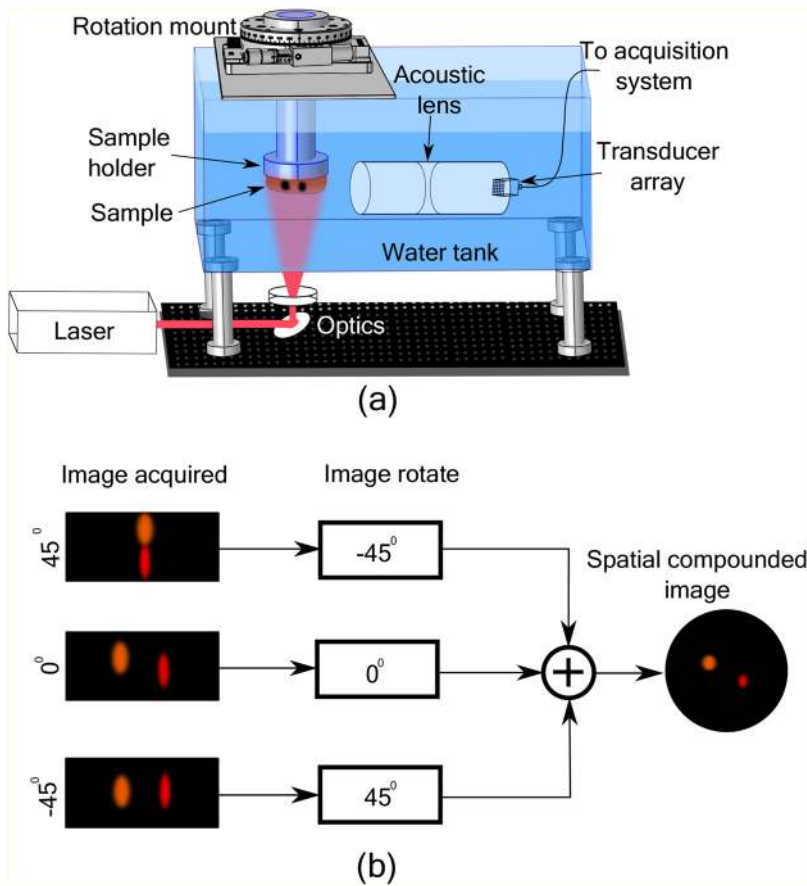


**Fig. 1.** (a) The setup for multiview spatial compounding using lens-based photoacoustic (PA) imaging system. The PA camera consisting of the lens and transducer array at  $2F$  distance, immersed in a water bath, with the center of phantom/tissue placed at approximately  $2F$  distance on the other side of the lens. An optical mirror and a beam expander were used to expand and uniformly illuminate the phantom from beneath. Multi-view PA signals were acquired by circularly rotating the phantom instead of the PA camera. (b) Cartoon examples of three angular views ( $-45^\circ$ ,  $0^\circ$  and  $45^\circ$ ) and the conceptual diagram of the SC process.

the final image. The final image possesses higher image quality compared to the single view sub-image [20,21]. As noted earlier, the PSF has an asymmetry with respect to the lens axis. This axis rotates as sub-image views are taken at different angles (see Fig. 1). For off-axis points and for planes other than best focus, the PSF remains rotated after the angle correction and registration of the sub-image. When averaged, this rotation effect contributes to the reduction of sidelobes in the lateral direction, resulting in improved PSF all around. This is notably different from  $360^\circ$  degree PA diffraction tomography where either with single or multi-element US transducers with wide reception angle one captures A-line signals by going around the object [22]. Then a model based delay-sum or filtered back projection algorithm has to be applied to reconstruct the final image. This is computationally more intensive compared to the simple sub-image averaging in our proposed SC.

### 2.3. Residual refocusing

This is a stand alone technique that was used by us on single view PA camera data. It was a simple matter to include this step on multi-view data before SC to study the incremental improvement in image quality. We provide a brief review of refocusing techniques used by researchers and explain the uniqueness of the method we have adopted. Refocusing using synthetic aperture methods with the delay and sum approach is used in US imaging [19]. A similar refocusing algorithm can be applied to transducer A-line data to bring all depths to its optimal focus. To keep the real-time nature of the imaging system, we have adopted a different approach, where a fast Fourier transform (FFT) based wave propagation model is used for residual refocusing. Kostil et al. [23] and Cox et al. [24] demonstrated an FFT based forward wave propagation and time reversal for PA imaging. In this model, the time series in A-line data can be mapped to a spatial location in the Fourier domain and both forward and inverse Fourier transform can be implemented in real-time using the FFT

algorithm which makes the model computationally less demanding than other reconstruction algorithms [25,26].

## 3. Methods

In this section, we present the acoustic lens design and PA system configuration used in this study. We further discuss the proposed residual refocusing for volumetric imaging and spatial compounding for lens-based PA imaging. We also provide both simulation and experimental setup details in this section.

### 3.1. Acoustic lens design and PA camera

The acoustic properties of soft tissue are mostly similar to water with sound speed around 1500 m/s. In designing the acoustic lens, water is considered as the propagating medium. Most of the solid lens making materials have a lower index of refraction and therefore a bi-concave lens is used for focusing. To make the lens making process inexpensive and easy, we have used 3D printing technology with a plastic material DSM18420 which has sound speed of 2590 m/s and density of  $884.17 \text{ kg/m}^3$  [27]. This provides a good impedance matching with water and enables more than 90% of the acoustic energy to pass through both sides of the lens [3]. The acoustic attenuation of the material is 5 MHz/dB/cm which provides an apodization effect, which is a desired effect in imaging applications using US transducer array. The focal length of the lens can be determined from the radius of curvature  $R$  and acoustic refractive index  $\mu = c_1/c_2$  given by,

$$\frac{1}{F} = (1 - \mu) \frac{2}{R}, \quad (3)$$

where  $c_1$  and  $c_2$  are the speed of sound in water and lens material respectively. We have considered a unit magnification system with object and image plane at  $2F$  distance from the center of the lens. For compact

imaging probe, we limited the total  $4F$  length of the system to 16 cm and diameter of the probe to 35 mm. So we arbitrarily choose the radius to be 33.5 mm to give a focal length of 39.8 mm. We choose the diameter of the lens as 32 mm. The lens was manufactured using a rapid prototype 3D printer which uses stereolithography technology at a resolution of 0.254–0.381 mm. Lens parameters for a specific resolution can be computed by the analysis presented in the reference [3].

### 3.2. Refocusing algorithm

The lens-based system has a fully focused object plane at distance  $2F$  from lens center. Consider a scenario where the focused object plane is passing through the center of the volume to be imaged. Then on either side of the focused plane, the time series gets defocused proportional to the distance. While the lens does the major focusing, a residual refocusing is needed for a uniform resolution throughout the imaging volume.

The residual refocusing algorithm is two folded as the transducer response has a fully focused time step at the center, and both sides need separate refocusing. Consider an initial photoacoustic pressure  $p_0(x, y, z)$  generated inside an object with the lens axis in the  $z$  direction. Let  $p(x, y, t)$  be the time series observed by the transducer. Further consider the fully focused object plane  $p_0(x, y, z = 2F)$  and the corresponding time sample as  $p(x, y, t = 2F)$ . Let  $p_0(x, y, z)_{2F-}$  denote pressure distribution for distances less than  $2F$  from the lens center and  $p_0(x, y, z)_{2F+}$  for depths beyond  $2F$ . The lens focuses the image of initial pressure  $p_0(x, y, z)_{2F-}$  beyond the image plane. However, it is detected before it reaches its optimal focus point. Similarly, the lens focuses the US waves propagated from initial pressure  $p_0(x, y, z)_{2F+}$  at a distance less than the image plane. This wavefront further propagates from its optimal focal point to reach the image plane. Hence, both  $p(x, y, t = 2F -)$  and  $p(x, y, t = 2F +)$  are unfocused with respect to its distance to optimal focal point.

The residual refocusing can be restated by eliminating the lens. The lens forms a volumetric image  $p_i(x, y, z)$  of the initial pressure  $p_0(x, y, z)$  with focused depths for each plane which is related by the lens equation ( $1/O + 1/I = 1/F$ ). In the restated problem we have a pressure profile  $p_i(x, y, z)$  with a imaging plane passing through the center ( $z = 0$ ) of the volume. Now the time series  $p(x, y, t)_{2F-}$  can be viewed as a wavefront generated from beyond the image plane and  $p(x, y, t)_{2F+}$  in front of the image plane. We can now consider the residual refocusing as measurements made by a planar detector array, separately for  $z = 0+$  and  $z = 0-$ . To keep the real-time nature of the system we use a FFT based wave propagation and time reversal method proposed by Kostil et al. [23] and Cox et al. [24]. In the frequency domain, the time series can be written as  $P(k_x, k_y, \omega) = \mathbb{F}\{p(x, y, t)_i\}$ , where  $\mathbb{F}\{\cdot\}$  is Fourier transform operation,  $i \in (2F -, 2F +)$ ,  $k_x$  and  $k_y$  are spatial wave number components,  $\omega$  is angular frequency and scaling factor  $\Gamma = c\sqrt{\omega^2 - c^2k_r^2}/2\omega$  with  $k_r = \sqrt{k_x^2 + k_y^2}$ . For a homogeneous medium, the angular frequency and the spatial wave number are related by the dispersion relation  $k_z = \sqrt{(\omega/c)^2 - k_r^2}$ . Using this dispersion relation the time series ( $t$ ) can be mapped to depth ( $z$ ) in the frequency domain by interpolating  $P(k_x, k_y, \omega)$  to  $P(k_x, k_y, k_z)$  [24].  $P(k_x, k_y, k_z)$  can now be transformed into spatial domain by performing inverse Fourier transform  $p(x, y, z) = \mathbb{F}^{-1}\{P(k_x, k_y, k_z)\}$ . In this way the whole imaging volume can be refocused using a fast post-processing step.

### 3.3. Spatial compounding

Fig. 1(a) shows the conceptual figure of a circular scanning lens-based PA imaging system. The target tissue is illuminated with a pulsed laser to form an initial pressure distribution. The pressure propagates outward in all directions, a portion of which gets intercepted by the lens which focuses the wavefront onto the transducer. After residual refocusing of the transducer time series, a single view of the target tissue is formed. If the target tissue is larger than the transducer area, then the whole lens along with the transducer is scanned in a 2D plane. The lens along with the transducer

can be rotated to a different angle to acquire the images from various angles. However, in this proof-of-concept study the sample holder was rotated. Again, the same procedure of laser illumination and imaging using the lens is repeated. After obtaining images from all desired angles, these images were rotated to the corresponding angle from where it was acquired. The rotated images are then interpolated to a larger uniformly spaced computational grid and summed to form the final image. Let  $p_{\theta_i}(x, y, z)$  be the limited image formed from a specific angle  $\theta_i$ . Given the measurements from  $N_\theta$  angular views, the final image was obtained by summing images from all angles,

$$P_{sc}(x, y, z) = \sum_{i=1}^{N_\theta} p_{\theta_i}(x, y, z). \quad (4)$$

### 3.4. Simulation setup

PSF studies were conducted using a simulation model of the lens based PA setup to mimic the experimental system. Simulations were carried out using PA MATLAB toolbox k-Wave [28]. A 2D computation grid of  $4 \text{ cm} \times 16 \text{ cm}$  was used for all the experiments. In order to support a maximum frequency of 7.5 MHz, a spacing of 0.025 mm was used in the grid. Since water is used as the medium, the background acoustic property was set to sound speed of 1500 m/s, density of  $1000 \text{ kg/m}^3$  and frequency dependent attenuation as 0.5 dB/MHz/cm. A biconcave lens was defined at the center of the imaging grid with sound speed of 2590 m/s, density of  $884.17 \text{ kg/m}^3$  and an attenuation of 5 dB/MHz/cm. The lens center thickness was taken to be 0.5 mm and radius of curvature as 33.5 mm. In order to image a larger phantom, the diameter was taken as 4 cm. The transducer array was placed in the model at  $2F$  distance from the lens center. The array had 20 elements, each having 2 mm sensing area and a pitch of 2.1 mm, with a center frequency of 3 MHz and 55% bandwidth at  $-6 \text{ dB}$ . Directional detectors were considered with weighted averaging of measurements from grid point inside the individual element area. Additive white noise at SNR level of 5 dB was added to the simulated A-line data acquired by each transducer element to study the change in SNR due to the proposed compounding method.

Two experiments were conducted in this simulation. In the first experiment, a single point source was defined as the initial pressure at  $2F$  distance from the lens center and using a first-order model the wave propagation through the medium and lens were mimicked. PSF measurements were made at the transducer location. The PSF thus obtained is then used for analyzing the effect of spatial compounding at different angles. In the second experiment, a phantom with nine different point targets along a line was defined to study the PSF variation at points in the front and behind the focal point. An initial simulation was carried out with the center of the phantom at  $2F$  distance from the lens and all point targets in line with the lens axis. Further, 35 more simulations were carried out with the phantom rotated at  $10^\circ$  in steps to simulate viewing of the sample from the entire  $360^\circ$ . Spatial compounding was performed by combining measurements from all the views to form the final image. More details of lens-based simulation setting can be found in our previous article [11].

### 3.5. Experimental setup

Phantom and *ex vivo* tissue imaging were conducted to show the usefulness of the proposed method. A tunable laser source EKSPLA Inc NT-352A, with 5 ns pulse at 10 Hz pulse repetition rate was used as the light source. An optical mirror and a beam expander lens combination were used to expand the 8 mm diameter laser beam to 4 cm diameter to illuminate the target. In all experiments the laser exposure was kept below  $16 \text{ mJ/cm}^2$ . The above mentioned 3D printed lens was used in the experiment. A 2D transducer array with 30 elements in a  $(5 \times 6)$  from IMASONIC, with an element size of  $2 \times 2 \text{ mm}$ . Multiple views of the target object were then acquired and then spatially compounded.

In the phantom study, a Polyvinyl chloride-plastisol (PVCP) phantom of 35 mm × 35 mm × 10 mm size with 5 graphite line targets (0.7 mm diameter and 10 mm long) was used as the sample. In the second experiment, a chicken kidney was used as a tissue sample. Two strong PA sources were created inside the tissue by injecting India ink into the tissue. For the phantom study the laser wavelength was set to 790 nm where graphite has high optical absorption and for tissue experiment it was set to 760 nm where Indian ink has peak absorption. Measurement procedure was similar to that of the phantom experiment. Acoustic measurements are made from the sides of the phantom (see Fig. 1) using the 2D transducer array, amplified and acquired using a custom developed simultaneous 32 channel DAQ system with variable gain (40–70 dB) and 30 MHz sampling rate 12 bit ADC.

## 4. Results

In this section, the results of the proposed PA imaging method are presented. First, we examine the change in resolution of the system with refocusing and cumulative spatial compounding at various angles in a simulation setting. We then demonstrate the advantage of the proposed method in phantom and tissue imaging.

### 4.1. Results from simulation study

A simulation study was used to answer three questions. First, how does the PSF for a point source located at the center of the rotation change with increasing angular compounding? Second, assuming that for the 0° view the center is in the best focal plane, what is the degree of PSF improvement for different off-focus planes in the front and back of this best focal plane due to 360 degree SC? Third, is there any incremental improvement in the final PSF if we add the refocusing step before SC? Answer to these questions are presented in Sections 4.1.1, 4.1.2 and 4.1.3 respectively.

#### 4.1.1. PSF at focal point with cumulative spatial compounding

At the best focal point with a single view of the point source, lateral FWHM was 3.83 mm and axial FWHM was 0.88 mm (PSF in Fig. 2(a)). This compares well with theoretical predictions of 3.27 mm and 0.85 mm respectively based on the PA camera model we described in our earlier paper [3]. A small difference in the lateral FWHM could be due to the fact that the theoretical prediction is for 3D while the simulation is 2D. Fig. 2(b) shows a change in lateral and axial FWHM with cumulative spatial compounding from 0° to 360° at a step size of 10°. The lateral FWHM drops to a value less than 1.5 mm with cumulative spatial compounding from 0° to 90° of angular coverage. The axial FWHM goes up slightly and approach lateral FWHM as the 2D PSF becomes more and more circularly symmetric. Beyond 90° both lateral and axial FWHM values show small oscillation around a mean 1.32 mm value while becoming equal 90°, 180°, 270° and 360°. A peak signal value of 0.078 was observed by the transducer at  $2F$  distance from the lens. With spatial compounding, the peak value is expected to improve. Fig. 2(c) shows a linear peak value improvement with cumulative spatial compounding. A rectangular box encapsulating  $-3$  dB points on lateral and axial PSF at the best focal point is used for SNR calculation. The ratio of the energy of PSF inside the rectangular box, normalized with its area to energy outside the box normalized with the area is used as SNR in this study. Fig. 2(c) shows SNR change with cumulative spatial compounding. Peak SNR was observed at spatial compounding of all 360° view. However, there is significant SNR gain with spatial compounding at lower angles. A cumulative compounding at 90° shows an SNR gain of 2 dB, 2.5 dB at 180° and 2.75 dB at 270° respectively. The final PSF with 360° SC is shown in Fig. 2(d).

The number of angular views for spatial compounding may be limited and tailored with respect to the imaging application. While small animal, breast imaging, etc. allows an entire 360° view, thyroid imaging may be limited by 140–170° view. One dimensional profile of

2D PSF along the lateral and axial direction at three different view angles 0°, 140° and full 360° is presented in Fig. 3. At 0°, lateral FWHM is 3.83 mm and axial FWHM is 0.88 mm. At 140°, PSF has lateral FWHM of 1.4186 mm and axial FWHM of 1.1710 mm. With full 360° view both lateral and axial FWHM attain a value of 1.32 mm.

#### 4.1.2. PSFs at off-focus points

As described in the section, simulated data was acquired from 9 point targets that were placed in line with the lens and transducer axis at different depth points as the phantom was rotated about the  $2F$  point. Simulations were carried out from 0° to 180° with angular steps of 10°. A direct spatial compounding performed with the observed PSFs from all the angles is shown in Fig. 4(b). Fig. 4(a) shows PSFs before SC at different off-focus points, ranging in distance from  $2F - 20$  mm to  $2F + 20$  mm in steps of 5 mm. PSFs after SC is shown in Fig. 4(b).

#### 4.1.3. PSF improvement with the addition of refocusing

In both experiments and simulations, the best focal point judged in terms of the smallest FWHM was observed at  $2F + 2.5$  mm for the transducer array location and not at  $2F$ . Hence, for all the simulations the transducer position was defined at  $2F + 2.5$  mm. The residual refocusing algorithm is then applied to time series data for each angular view. PSFs corresponding to 9 point sources after refocusing are shown in Fig. 4(c). SC was then performed using the refocused multi-view data. Fig. 4(d) shows the improvement in PSFs after refocusing and spatial compounding.

A quantitative comparison based on FWHM and SNR improvement is presented in Fig. 5(a) and (b). Uncorrelated additive white noise of SNR 10 dB was added to the measurement at each view. SNR was computed by considering a patch for signal and remaining part as noise. The patch size was considered to encapsulate  $-3$  dB point of the best PSF. The energy in the patch was then estimated and normalized with the area. In a similar fashion, all energy outside the patch normalized with the area was considered as the noise component. SNR was then estimated by taking the ratio of the signal component to that of noise. Lateral FWHM and SNR improved significantly with refocusing and spatial compounding. Let us consider two representative points,  $2F - 20$  mm and  $2F$  to see the effect of refocusing and spatial compounding. At  $2F - 20$  mm with single view lateral FWHM is 6.95 mm, while with simple spatial compounding it improves to 2.56 mm. After refocusing lateral FWHM was 3.96 mm and with compounding the best FWHM of 1.84 mm is achieved. While lateral FWHM improves significantly axial FWHM degrades slightly so that both the lateral and axial resolutions converge. Initial axial FWHM was 0.87 mm and after refocusing it becomes 0.90 mm. After spatial compounding FWHM without and with refocusing are 1.17 mm and 1.65 mm respectively. SNR at  $2F - 20$  mm is  $-3.16$  dB and with spatial compounding, a gain of 0.87 dB was observed while refocusing resulting in a gain of 1.71 dB was observed for refocusing. With combined refocusing and spatial compounding, a gain of 1.81 dB was obtained. The PSF corresponding to  $2F$  depth has a lateral FWHM of 3.84 mm, and after spatial compounding, it improves to 1.55 mm. With refocusing there is slight resolution enhancement with lateral FWHM being 3.65 mm which then combined with spatial compounding yields the best PSF of 1.31 mm. Corresponding axial FWHM value at  $2F$  is 0.88 mm. Refocusing does not have any impact on axial FWHM. With spatial compounding, axial FWHM approached a value of 1.31 mm. At  $2F$ , the initial SNR was measured to be  $-2.12$  dB, with refocusing and spatial compounding a gain of 1.04 dB and 1.73 dB was observed respectively.

## 4.2. Imaging experiments

With the experimental setup explained above, phantom and tissue imaging experiments were conducted. The volumetric data obtained from each angle was then combined using refocusing and spatial compounding to form the final image. The sampling rate of the acquisition system is 30 MS/s while the pitch of the transducer is 2.1 mm. To

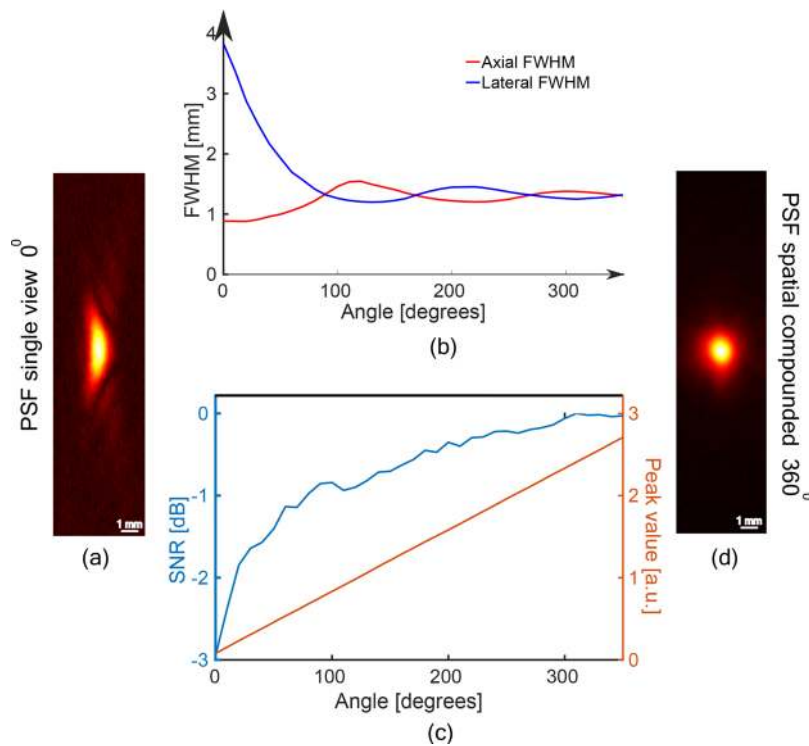


Fig. 2. (a) PSF at the focal point with a single view ( $0^\circ$ ), (b) axial and lateral Full Width at Half Maximum (FWHM) change with cumulative spatial compounding, (c) Signal to Noise Ratio (SNR) and peak value change with cumulative spatial compounding (d) PSF after spatial compounding over ( $360^\circ$ ).

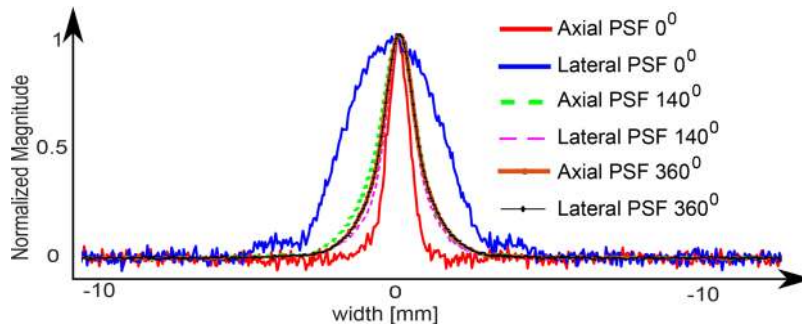


Fig. 3. Demonstration of Point Spread Function (PSF) varying from single view imaging to multiple view imaging. Axial and lateral PSF at single view ( $0^\circ$ ), with spatial compounding from  $0^\circ$  to  $140^\circ$  at  $10^\circ$  steps and with spatial compounding from  $0^\circ$  to  $360^\circ$  at  $10^\circ$ .

rotate the acquired image to a specific angle and to perform spatial compounding an equispaced grid is required. Hence, the acquired data was resampled with linear interpolation to an equispaced grid of 0.1 mm spacing before spatial compounding. In the phantom experiment five line targets in a polymer phantom were imaged. Fig. 6(a) shows the photograph of the phantom used for imaging. Fig. 6(b)–(d) shows PA images obtained from a single view of the target from  $0^\circ$ ,  $45^\circ$  and  $90^\circ$  respectively. For all the line targets which are viewed fully by the PA camera at a given angle the lateral and axial FWHM were calculated. The lateral FWHM of the line targets varied from 2.7 mm to 4.8 mm with a mean value of 3.2 mm while the axial resolution is approximately 0.8 mm for all the targets. After spatial compounding, the central target is mostly symmetric with both axial and lateral resolution being  $2.8 (\pm 0.3)$  mm. With spatial compounding from partially imaged targets resulted in asymmetry in four targets away from the center. The resolution of the targets away from the center varied from 0.9 mm to 2.4 mm. However, it can be observed that there is an improvement in resolution with spatial compounding even with partially imaged targets. Fig. 6(e) shows an exploded view of the combined image along the  $xy$ ,  $xz$  and  $yz$  planes with respect to the center of the

phantom. Fig. 6(f) shows the 3D image displaying all five line targets.

*Ex vivo* tissue imaging was conducted using chicken kidney with Indian ink injected at two spots inside the tissue. Imaging similar to that in the phantom was carried out here. Fig. 7(a) shows photographs of the tissue with Indian ink spots marked using a circle. Fig. 7(b)–(d) shows single view of the tissue from  $0^\circ$ ,  $45^\circ$  and  $-45^\circ$  respectively. Fig. 7(e) shows the combined 2D PA image of the tissue and Fig. 7(f) shows the volumetric PA image after combining images from all angles.

### 5. Discussion

The proposed spatial compounding using lens-based PA imaging provides multiple benefits over single view imaging. In a single view with multiple targets at different depths, the PSF in the best focal plane at  $2F$  has an optimal resolution, but it begins to degrade in-depth planes behind and in front of the  $2F$  plane. This degradation is predominantly characterized by an increase in lateral FWHM with increasing distance from the  $2F$  plane (Fig. 5(a)), while the axial FWHM does not change much. In a single view, the asymmetric nature of the PSF remains in all depths planes because the lateral FWHM is always much larger than

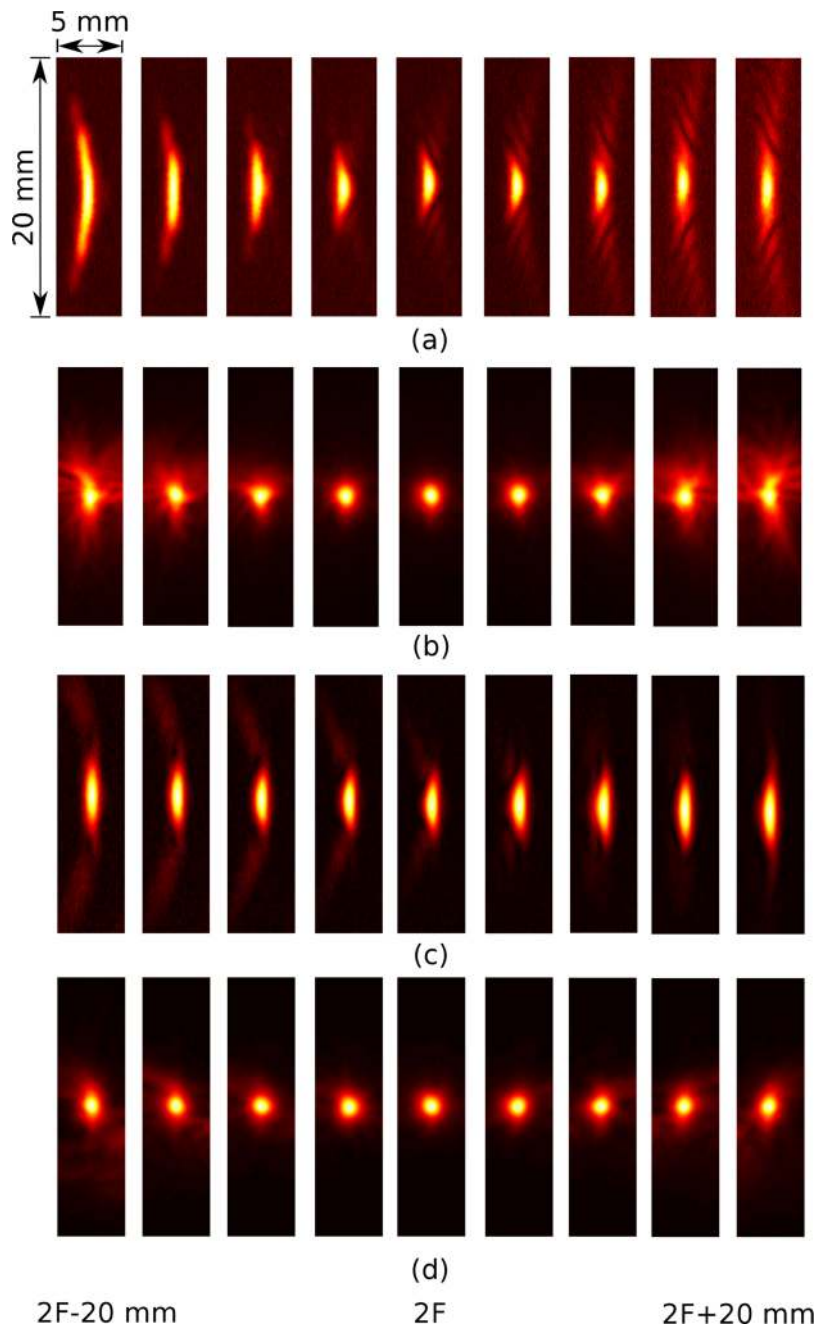


**Fig. 4.** PSF at different depths from  $2F - 20$  mm to  $2F + 20$  mm with 5 mm step. (a) Viewed from  $0^\circ$ . (b) PSFs after cumulative spatial compounding without refocusing. (c) PSFs after applying the refocusing algorithm. (d) PSFs after cumulative spatial compounding with refocusing.

axial FWHM (see Fig. 4(a)). Simulation of multiple views followed by spatial compounding demonstrates that PSF in all depths planes is rendered nearly symmetric. The FWHM of this symmetric PSF has many fold improvement over the single view lateral FWHM in the corresponding PSFs at different depth planes (see Fig. 4). For example, the asymmetric PSF at a depth plane 2 cm behind the  $2F$  plane has a lateral FWHM of 7 mm vs. 4 mm at  $2F$  plane in a single view image that gets reduced to symmetric PSF with FWHM of 2.5 mm and 1.6 mm respectively after spatial compounding with  $360^\circ$  angular data.

Simulation study also sheds some light on how the changes in the PSF progress with cumulative angular compounding. From Fig. 3, averaging  $90^\circ$  angular views, the lateral FWHM of the PSF at  $2F$  has decreased from 4 mm to 1.32 mm, while the axial FWHM increases slightly from 0.8 mm to 1.32 mm. In this way the overall system resolution was improved beyond the transducer aperture with a tradeoff

on the axial resolution. Beyond  $90^\circ$ , both lateral and axial FWHM converge, oscillating periodically with maximum axial FWHM to lateral FWHM variation of 0.2 mm. It is interesting to see that at  $90^\circ$ ,  $180^\circ$ ,  $270^\circ$  and  $360^\circ$  both lateral and axial resolutions converge making these views ideal for uniform circularly symmetric resolution. This analysis shows that for imaging applications using a lens based system with a limited view, a resolution close to the best possible resolution predicted by the system parameters can be achieved. In applications like breast tissue imaging and small animal studies the entire  $360^\circ$  view is possible, while in the case of thyroid imaging, only a limited view is available. Given the thyroid anatomy, a plausible assumption is that  $140^\circ$  view is feasible. In one example,  $172^\circ$  has been used [29].

Concomitant to the PSF improvement, there is a modest square root of  $N$  improvement in SNR with spatial compounding, where  $N$  is the number of angular frames that are averaged. This is evident from the

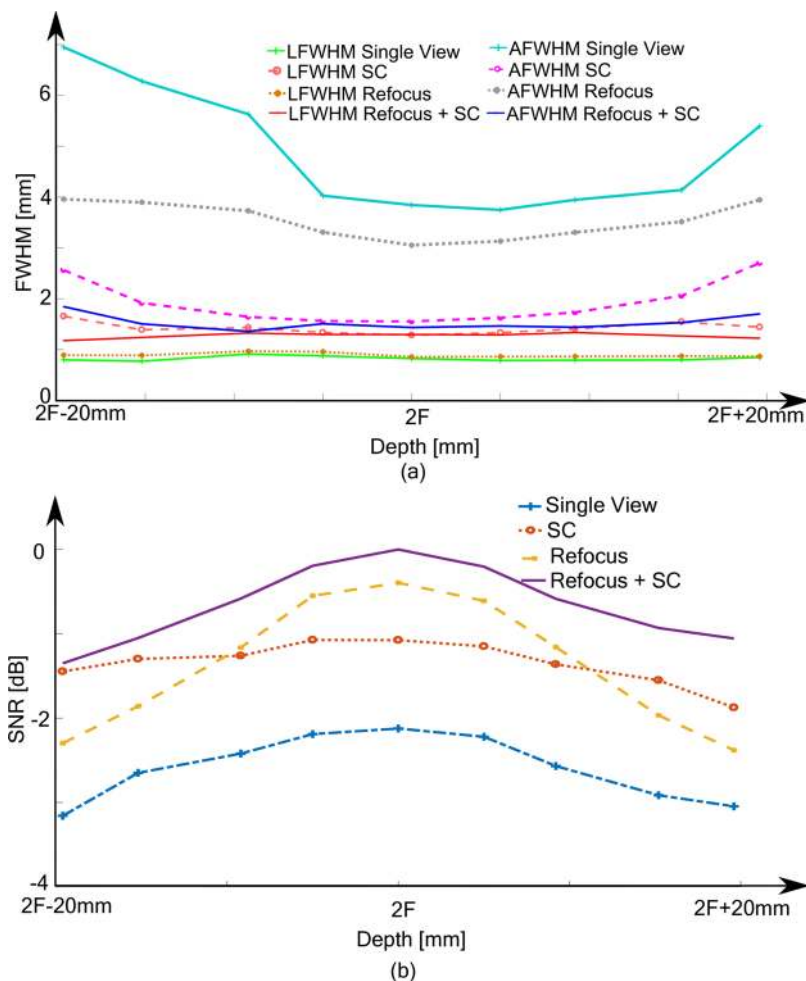


Fig. 5. (a) Axial-FWHM (A-FWHM) and lateral-FWHM (L-FWHM) change with cumulative spatial compounding at different depths shown in Fig. 4 for the single view, spatial compounding (SC) without refocusing and SC with refocusing, (b) Signal to Noise Ratio (SNR) for the single view, SC without refocusing and SC with refocusing.

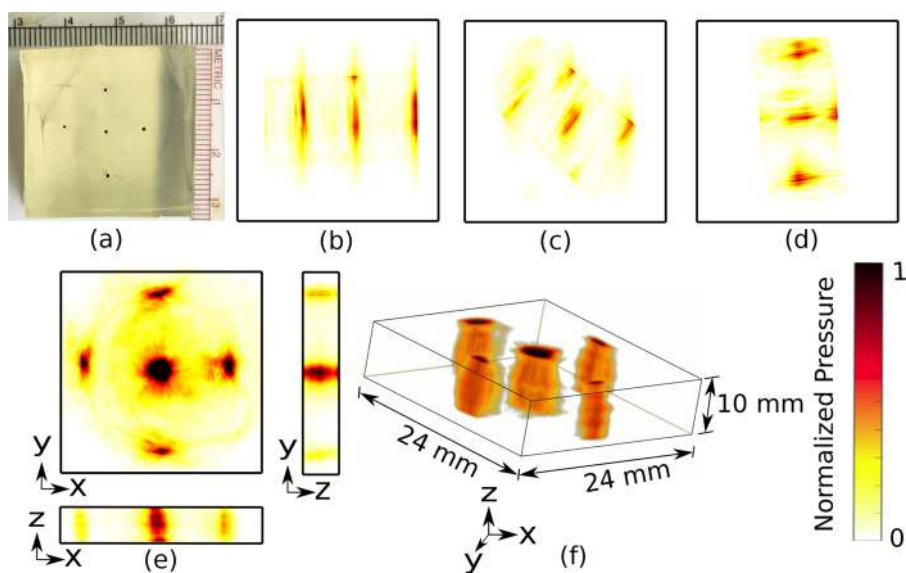
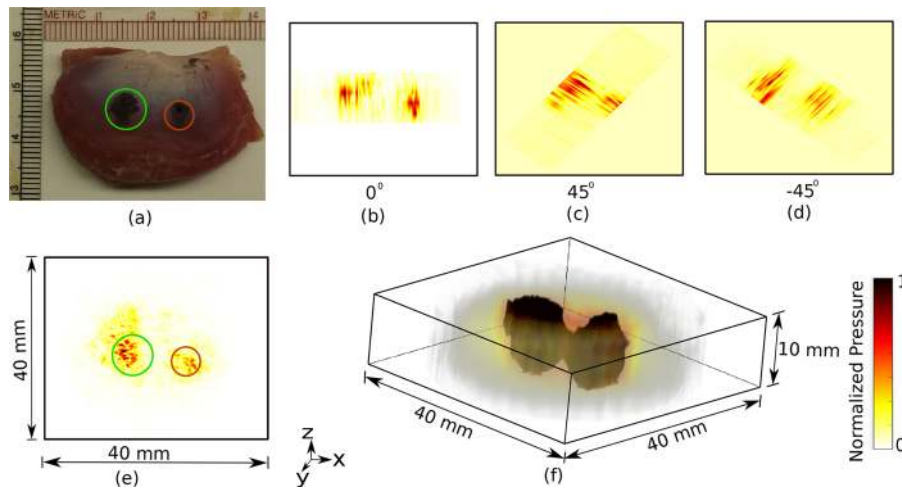


Fig. 6. (a) Photograph of the imaged phantom. Single view photoacoustic (PA) image at (b) 0°, (c) 45° and (d) 90°. (e) Exploded view (xy, xz and yz) of PA image after spatial compounding from all angles. (f) Volumetric PA image of phantom after spatial compounding.





**Fig. 7.** Imaging a chicken tissue with two Indian ink spots. (a) Photograph of the imaged chicken tissue. Single view PA image at (b)  $0^\circ$ , (c)  $45^\circ$  and (d)  $-45^\circ$ . (e) Cross section ( $xy$ ) photoacoustic (PA) image of tissue after spatial compounding. (f) Volumetric PA image of tissue after spatial compounding.

linear increase in peak signal value and the non-linear SNR increase in Fig. 2(b). This type of SNR improvement occurs even in single view PA image when multiple frames acquired from several independent laser firings are averaged, though there will not be any PSF improvement in this case. Therefore there is a dual benefit in multiview PA camera-based data acquisition and SC. We significantly improve the PSF everywhere within the imaged volume along with modest improvement in SNR. For a clinical *in-vivo* system this should be easy to implement because high powered lasers typically used for PA imaging have pulse repetition rate on the order of a few tens of Hertz. This should provide enough time to rotate the gantry before the next laser firing. The questions regarding laser delivery to the target organ were not considered in this prototype system design. Hence laser absorption losses were ignored in both experimental and simulated data analysis. Therefore, in a more realistic situation, SNR improvement may differ.

Our proposed re-focusing algorithm provides an additional improvement to the PSF when it is combined with SC [17]. If it is applied alone after the PA camera data is acquired, the PSF gets equalized at all depths, approaching its best value at  $2F$  (see Fig. 4(c)). Specifically, at off-focal planes, the lateral FWHM shrinks to varying degree but axial FWHM does not change much (see Fig. 5(a)). As a result, PSF remains asymmetric. Furthermore, lateral FWHM still remains worse than SC result (approximately 4 mm vs. 2 mm). If we apply re-focusing to all the multi-view data and then perform spatial compounding, we get circularly symmetric, almost spatially uniform PSF, with the best possible FWHM of 1.6 mm. Therefore, if multi-angle viewing is not practical, just applying the re-focusing algorithm to the PA camera data is worthwhile because lateral FWHM can be improved from spatially varying 4–7 mm to approximately spatially uniform 4 mm. It is important to note that all these resolution numbers are highly dependent on lens parameters and US transducer element size and bandwidth, as discussed in detail in our earlier article [3]. The PA camera resolution is much worse than the previous design [3] mainly because we increased the transducer element size from  $1\text{ mm} \times 0.5\text{ mm}$  to  $2\text{ mm} \times 2\text{ mm}$  and decreased the center frequency from 5 MHz to 3 MHz. This was done to increase the system sensitivity and PA imaging penetration depth for *in-vivo* imaging. With the application of the techniques discussed in this article, we can regain most of the resolution loss without compromising on the overall system sensitivity.

In the light of the PSF improvements demonstrated by simulations, we can appreciate and understand the improvements seen in the phantom and tissue PA imaging results. In Fig. 6(b), the 0 degree single view, the asymmetry between lateral and axial profiles of all the point targets in the B-scan (cross-sectional brightness scan perpendicular to the imaging plane) image is evident. The signal intensity varies, probably because the laser exposure in the expanded beam was not spatially uniform. After  $360^\circ$

spatial compounding, in Fig. 6(e) the PA images of all 5 sources in the B-scan have become approximately circular with a much tighter cross-sectional profile. 3D rendering in Fig. 6(f) qualitatively shows that 10 mm long and 0.7 mm diameter lead sources have been imaged well without the spatially non-uniform blurring expected from single view PA camera imaging. Single view images of the tissue from different angles (Fig. 7(b)–(d)) show a wider lateral spread for the two Indian ink spots and a non-uniform spatial resolution. Fig. 7(e) is a C-scan slice in the  $xy$  plane taken at 5 mm depth in the tissue. The two smooth circles are drawn on Fig. 7(a) and (e) mark the spot of the ink injection. From the tight small spots we can visualize that within the circle in Fig. 7(e) are probably indicative of high-resolution mapping of inhomogeneous ink distribution within the injected spot. Fig. 7(f) is a 3D image rendering that clearly shows the two ink injection spots with the tissue volume. The SNR gain is also high as the region of interest significantly improves with compounding. Both phantom and tissue experiments highlight the efficacy of spatial compounding in improving SNR and resolution.

## 6. Conclusions

A simple SC process that works only with the multi-view data acquired with our lens-based focusing PA camera is shown to render the system PSF almost circularly symmetric and produce a two-fold improvement in lateral resolution. A fast refocusing algorithm is shown to equalize the non-symmetric PSF at all depths within the imaging volume. Combining both these techniques can provide a spatially uniform and circularly symmetric high resolution throughout a small imaging volume. In addition to the high resolution, the process is also shown to improve the SNR of the image. The proposed method has potential applications in situations where multiple views of the target tissue are possible, such as thyroid, breast and small animal imaging.

## References

- [1] K.S. Valluru, K.E. Wilson, J.K. Willmann, Photoacoustic imaging in oncology: translational preclinical and early clinical experience, *Radiology* 280 (2016) 332–349.
- [2] K. Valluru, B. Chinni, S. Bhatt, V. Dogra, N. Rao, D. Akata, Probe design for photoacoustic imaging of prostate, *IEEE International Conference on Imaging Systems and Techniques* (2010) 121–124.
- [3] K.J. Francis, B. Chinni, S.S. Channappayya, R. Pachamuthu, V.S. Dogra, N. Rao, Characterization of lens based photoacoustic imaging system, *Photoacoustics* 8 (2017) 37–47.
- [4] Y. He, Z. Tang, Z. Chen, W. Wan, J. Li, A novel photoacoustic tomography based on a time-resolved technique and an acoustic lens imaging system, *Phys. Med. Biol.* 51 (2006) 2671.
- [5] H. Zhang, Z. Tang, Y. He, L. Guo, Two dimensional photoacoustic imaging based on an acoustic lens and the peak-hold technology, *Rev. Sci. Instrum.* 78 (2007)

064902.

- [6] W. Wan, R. Liang, Z. Tang, Z. Chen, H. Zhang, Y. He, The imaging property of photoacoustic Fourier imaging and tomography using an acoustic lens imaging system, *J. Appl. Phys.* 101 (2007) 063103.
- [7] Y. Wei, Z. Tang, H. Zhang, Y. He, H. Liu, Photoacoustic tomography imaging using a 4f acoustic lens and peak-hold technology, *Opt. Express* 16 (2008) 5314–5319.
- [8] V.S. Dogra, B.K. Chinni, K.S. Valluru, J. Moalem, E.J. Giampoli, K. Evans, N.A. Rao, Preliminary results of ex vivo multispectral photoacoustic imaging in the management of thyroid cancer, *Am. J. Roentgenol.* 202 (2014) W552–W558.
- [9] S. Sinha, V.S. Dogra, B.K. Chinni, N.A. Rao, Frequency domain analysis of multi-wavelength photoacoustic signals for differentiating among malignant, benign, and normal thyroids in an ex vivo study with human thyroids, *J. Ultrasound Med.* 36 (2017) 2047–2059.
- [10] V.S. Dogra, B.K. Chinni, K.S. Valluru, J.V. Joseph, A. Ghazi, J.L. Yao, K. Evans, E.M. Messing, N.A. Rao, Multispectral photoacoustic imaging of prostate cancer: preliminary ex-vivo results, *J. Clin. Imaging Sci.* 3 (2013).
- [11] B. Chinni, Z. Han, N. Brown, P. Vallejo, T. Jacobs, W. Knox, V. Dogra, N. Rao, Multi-acoustic lens design methodology for a low cost C-scan photoacoustic imaging camera, *Photons Plus Ultrasound: Imaging and Sensing 2016*, vol. 9708, International Society for Optics and Photonics, 2016 p97081Q.
- [12] J. Niederhauser, M. Jaeger, M. Frenz, Real-time three-dimensional photoacoustic imaging using an acoustic lens system, *Appl. Phys. Lett.* 85 (2004) 846–848.
- [13] X. Chen, Z. Tang, Y. He, H. Liu, Y. Wu, A simultaneous multiple-section photoacoustic imaging technique based on acoustic lens, *J. Appl. Phys.* 108 (2010) 073116.
- [14] E. Jen, H. Lin, H.K. Chiang, 4th International Conference on Biomedical Engineering and Informatics (BMEI), 3D photoacoustic imaging system with 4F acoustic lens, 1 2011, pp. 5–7.
- [15] K.S. Valluru, B.K. Chinni, N.A. Rao, et al., Photoacoustic imaging: opening new frontiers in medical imaging, *J. Clin. Imaging Sci.* 1 (2011) 24.
- [16] N. Rao, K.J. Francis, B. Chinni, Z. Han, V. Dogra, Innovative approach for including dual mode ultrasound and volumetric imaging capability within a medical photoacoustic imaging camera system, *Optical Tomography and Spectroscopy*, Optical Society of America, 2018 OW4D-2.
- [17] K.J. Francis, B. Chinni, S.S. Channappayya, R. Pachamuthu, V.S. Dogra, N. Rao, Two sided residual refocusing for acoustic lens based photoacoustic imaging system, *Phys. Med. Biol.* 63 (13) (2018) 13TN03.
- [18] M.C. Hemmsen, J.H. Rasmussen, J.A. Jensen, Tissue harmonic synthetic aperture ultrasound imaging, *J. Acoust. Soc. Am.* 136 (2014) 2050–2056.
- [19] J. Opretzka, M. Vogt, H. Ermert, A high-frequency ultrasound imaging system combining limited-angle spatial compounding and model-based synthetic aperture focusing, *IEEE Trans. Ultrason. Ferroelectr. Freq. Control* 58 (2011).
- [20] J. Park, J.B. Kang, J.H. Chang, Y. Yoo, Speckle reduction techniques in medical ultrasound imaging, *Biomed. Eng. Lett.* 4 (2014) 32–40.
- [21] H.J. Kang, M.A.L. Bell, X. Guo, E.M. Boctor, Spatial angular compounding of photoacoustic images, *IEEE Trans. Med. Imaging* 35 (2016) 1845–1855.
- [22] L.V. Wang, S. Hu, Photoacoustic tomography: in vivo imaging from organelles to organs, *Science* 335 (2012) 1458–1462.
- [23] K.P. Köstli, M. Frenz, H. Bebie, H.P. Weber, Temporal backward projection of photoacoustic pressure transients using fourier transform methods, *Phys. Med. Biol.* 46 (2001) 1863.
- [24] B. Cox, P. Beard, Fast calculation of pulsed photoacoustic fields in fluids using *k*-space methods, *J. Acoust. Soc. Am.* 117 (2005) 3616–3627.
- [25] K. Wang, M.A. Anastasio, A simple Fourier transform-based reconstruction formula for photoacoustic computed tomography with a circular or spherical measurement geometry, *Phys. Med. Biol.* 57 (2012) N493.
- [26] C. Lutzweiler, D. Razansky, Photoacoustic imaging and tomography: reconstruction approaches and outstanding challenges in image performance and quantification, *Sensors* 13 (2013) 7345–7384.
- [27] S. DSM Functional Materials, Protogen 18420, <https://www.dsm.com/corporate/home.html> (last accessed: October 2018).
- [28] B.E. Treeby, B.T. Cox, *k*-wave: Matlab toolbox for the simulation and reconstruction of photoacoustic wave fields, *J. Biomed. Opt.* 15 (2010) 021314.
- [29] A. Dima, V. Ntziachristos, In-vivo handheld photoacoustic tomography of the human thyroid, *Photoacoustics* 4 (2016) 65–69.



**K.J. Francis** graduated in Electronics and Communication Engineering from Calicut University in 2011. He received his master degree in Communication and Signal Processing from Christ University in 2013. He is a Fulbright-Nehru doctoral researcher at Rochester Institute of Technology. He completed his Ph.D. degree from Indian Institute of Technology, Hyderabad in 2018. He is currently working as a postdoctoral researcher at the University of Twente. His research interest lies in medical imaging. Presently, his research focus is in developing a photoacoustic system for interventional procedures.



**Bhargava Chinni** is a Master of Science graduate in Electrical Engineering from Rochester Institute of Technology, NY, USA. His primary research interests include data analytics, photoacoustic imaging, computer vision, signal and image processing.



**Sumohana Channappayya** received his Ph.D. degree in ECE from the University of Texas at Austin in 2007. He is currently Associate Professor of Electrical Engineering at the Indian Institute of Technology Hyderabad. His research interests include image and video quality assessment, biomedical imaging and image processing.



**P. Rajalakshmi** received her Ph.D. degree in Electrical Engineering from the Indian Institute of Technology, Madras in 2009. She is currently Associate Professor of Electrical Engineering at the Indian Institute of Technology Hyderabad. Her research interests include Wireless Communication, Wireless Sensor Networks, Embedded Systems, Cyber Physical Systems/Internet of Things, Green Communications, and Ultrasound Imaging.



**Vikram S. Dogra**, MD Professor of Radiology, Urology, and Biomedical Engineering at the University of Rochester School of Medicine in Rochester, NY as well as affiliate Professor of Imaging Science at Rochester Institute of Technology. Applications of ultrasound and Photo-acoustic imaging for clinical diagnosis and research are his main passion. His special skills include organizational capacity, leadership, and depth of clinical knowledge in applications of ultrasound and problems faced in the cancer detection.



**Naval Gund Rao** received his Ph.D. degree in Physics from University of Minnesota in 1979. After working as a Post-doc at Ohio State University, a geophysicist at Shell Oil Company and NIH fellow at Colorado Health Science center, he has been an Imaging Science professor at Rochester Institute of Technology for the past 29 years. His research interests are in medical Ultrasound and Photoacoustic Imaging and spectroscopy and the development of new imaging technologies and image processing methodologies.